HHS Public Access

Author manuscript

Nat Neurosci. Author manuscript; available in PMC 2015 October 01.

Published in final edited form as:

Nat Neurosci. 2015 April ; 18(4): 511–520. doi:10.1038/nn.3953.

Selective inhibitors of nuclear export avert progression in preclinical models of inflammatory demyelination

Jeffery D. Haines, PhD[1], **Olivier Herbin, PhD**[2], **Belén de la Hera**[1], **Oscar G. Vidaurre, MD, PhD**[1], **Gregory A. Moy**[1], **Qingxiang Sun, PhD**[3], **Ho Yee Joyce Fung**[3], **Stephanie Albrecht**[4], **Konstantina Alexandropoulos, PhD**[2], **Dilara McCauley, PhD**[5], **Yuh Min Chook, PhD**[3], **Tanja Kuhlmann, MD, PhD**[4], **Grahame J. Kidd, PhD**[6], **Sharon Shacham, PhD**[5], and **Patrizia Casaccia, MD, PhD**[1,*]

[1]Department of Neuroscience and Genetics and Genomics, Icahn School of Medicine at Mount Sinai, New York, NY, USA.

[2]Department of Medicine, Division of Clinical Immunology, The Immunology Institute, Icahn School of Medicine at Mount Sinai, New York, NY, USA.

[3]Department of Pharmacology, University of Texas Southwestern Medical Center, 6001 Forest Park Road, Dallas, TX 75390-9041.

[4]Institute of Neuropathology, University Hospital Münster, Pottkamp 2, 48149 Münster, Germany.

[5]Karyopharm Therapeutics, 2 Mercer Road, Natick, MA 01760, USA.

[6]Department of Neurosciences, Cleveland Clinic, 4500 Euclid Ave, Cleveland, OH, 44195, USA.

Abstract

Axonal damage has been associated with aberrant protein trafficking. This study characterizes a novel class of compounds targeting nucleo-cytoplasmic shuttling, by binding to the catalytic groove of the nuclear export protein XPO1/CRM1 (chromosome region maintenance protein1). Oral administration of novel reversible CRM1 inhibitors in preclinical murine models of demyelination significantly attenuated disease progression, even when started after the onset of paralysis. Clinical efficacy was associated with decreased proliferation of immune cells, characterized by nuclear accumulation of cell cycle inhibitors, and preservation of cytoskeletal integrity even in demyelinated axons. Neuroprotection was not limited to models of

*To whom correspondence should be addressed: Patrizia Casaccia MD, PhD., Icahn School of Medicine at Mount Sinai, 1425 Madison Ave., Box 10-65, New York, NY, 10029. Tel: 212-659-5988, Fax: 212-996-9785, patrizia.casaccia@mssm.edu.

Author Contributions: PC, SS, JDH, and DM were responsible for overall analysis and study design. In vivo and in vitro experiments were performed by JDH, OH, BHH, OGV, GAM. QS, HYJF and YMC crystallized Crm1 bound to SINE and performed gel shift assays. SA and TK performed the human brain immunohistochemistry experiments. GJK helped analyze and interpret the three-dimensional electron microscopy results. Immunology experiments were conceived and interpreted by OH and KA. Pharmacokinetic experiments and characterization of drug properties were performed by DM and SS. The paper was written by JDH and PC.

Competing interests: SS and DM are currently employed at and hold leadership positions at Karyopharm Therapeutics, they also hold stock in the company.

Data and materials availability: The KPT compounds are available through Karyopharm Therapeutics through an MTA and are not archived.

demyelination, but observed also in other mouse models of axonal damage (i.e. kainic acid injection) and detected in cultured neurons after knockdown of *Xpo1*, the gene encoding for CRM1. A proteomic screen for target molecules revealed that CRM1 inhibitors in neurons prevented nuclear export of molecules associated with axonal damage while retaining transcription factors modulating neuroprotection.

INTRODUCTION

Focal axonal damage (FAD) is a pathological hallmark of neurodegenerative disorders including Alzheimer's, amyotrophic lateral sclerosis and multiple sclerosis[1,2]. It is characterized by cytoskeletal disruption and impaired axonal transport, resulting in localized axonal swellings[1,3]. Dysregulated nucleo-cytoplasmic shuttling is one of the mechanisms hypothesized to contribute to the pathogenesis of this localized damage in several neurological disorders[4-6]. For this reason, we tested whether targeting nuclear transport could be considered a novel venue of therapeutic intervention with potentially broad implications for neurodegenerative diseases. We previously identified exportin 1 (XPO1/CRM1)-mediated nuclear export as necessary for FAD[4]. CRM1 is a member of the nuclear export family of proteins that recognizes cargoes containing leucine-rich nuclear export sequences[7] and transports them from the nucleus to the cytoplasm[8-10]. Neurotoxicity has been associated with the accumulation in the axoplasm of molecules interfering with axonal cytoskeleton such as TAU [11] and RNA transport such as FUS and TDP-43[12-14], thereby triggering the onset of focal axonal damage. Alternative pathogenetic explanations have focused on the decreased nuclear localization of NRF2 (nuclear factor (erythroid-derived 2)-like 2) a transcription factor involved in anti-oxidant defense [15-18]. However – to date – the potential therapeutic value of targeting nucleo-cytoplasmic export has not been explored. This study directly addresses this outstanding question, by characterizing the structure and biological activity of compounds targeting the nuclear export protein CRM1. We also report their beneficial therapeutic role in two pre-clinical models of axonal damage in the context of autoimmune demyelination and in a model of neurotoxicity following kainic acid injection. Finally, using proteomic approaches, we identify nuclear retention of protein targets that have been implicated in the pathogenesis of other neurological disorders, thereby rendering the CRM1 inhibitors potentially suitable candidates for the development of therapeutic strategies broadly targeting neuroprotection.

RESULTS

CRM1 protein levels are upregulated in human MS brains

Previous data from our lab revealed aberrant localization of nuclear protein in axons characterized by focal axonal damage in MS brains[4]. An important regulator of nucleo/cytoplasmic shuttling is the exportin1 protein CRM1 [8-10] we therefore sought to define the pattern of expression of CRM1 by immunohistochemistry of leukocortical MS brain lesions. Actively demyelinating lesions were defined on the basis of the reduced immunoreactivity to antibodies specific for myelin basic protein (MBP) both in the white and gray matter (Fig 1a), the presence of phagocytes containing MBP-positive myelin degradation products within the cytoplasm at the lesion border (insert in Fig. 1a) and the presence of numerous

foamy phagocytes expressing CD68. In the adjacent demyelinated gray matter, numerous NeuN+ neurons were present, some of them with peri-somatic neurofilament immunopositivity, suggestive of neuronal damage (Fig 1b). The density of CD68+ cells was lower in the cortical lesion area compared to the white matter (Fig. 1a-b). CRM1 expression was detected in both immune and neuronal cells. Within the demyelinating white matter lesion CRM1 expression was elevated in infiltrating CD45+ perivascular cells (Fig. 1c). In the demyelinated as well as in the normal appearing gray matter CRM1 immunoreactivity was detected in neurons (Fig. 1d-e). Western blot analysis of protein extracts from MS cortical gray matter (n = 8), further revealed an 80% increase (**p = 0.0081) of CRM1 protein levels compared to matched non-neurological controls (n = 5) (**Fig. 1e, Table 1**). Together these results led us to propose that targeting nucleo-cytoplasmic shuttling by modulating CRM1 activity could be explored as potential new therapeutic strategy for axonal damage in demyelinating disorders.

Characterization of novel inhibitors of CRM1

Of several molecules targeting the catalytic groove of CRM1, KPT-276 and KPT-350 were two of the lead inhibitors, structurally defined by a difluoroazetidinepropenonenyl group, which significantly differed from other published inhibitors, including leptomycin B[19,20]. Both KPT-276 and KPT-350 share a trifluoromethyl phenyl triazole scaffold (**Fig. 2a**), with previously reported compounds KPT-185[21] and KPT-251[22] (**Supplementary Fig. 1a-c**). *In vitro*, KPT-276 was capable of disrupting Ran-dependent CRM1 binding to NES of the protein kinase A inhibitor protein (PKI) (**Fig. 2b**), a *bona fide* NES-containing CRM1 target. The 1.8 Å resolution crystal structure of KPT-276 bound to CRM1, revealed covalent conjugation of the inhibitor to the reactive cysteine residue in the NES-binding groove of CRM1 and a binding mode similar to that of KPT-185 and KPT-251 (Cys539 in a modified yeast CRM1) (**Fig. 2c-d; Table 2**). KPT-276 had a molecular weight of 426.27 g/mol, a partition coefficient of 4.44, and a topological polar surface area of 48.27 (**Fig. 2e**). KPT-350 a related and more potent CRM1 inhibitor was characterized by a molecular weight of 449.35 g/mol, a partition coefficient of 3.48, and a topological polar surface area of 86.16. The two inhibitors were designed for oral administration and had the ability to cross the blood-brain barrier with different partition coefficients between blood plasma and the parenchyma as determined by pharmacokinetic measurements in rats (**Fig. 2f**). When tested against an extensive panel of 150 different kinases, and phosphatases no binding was seen (data not shown), further supporting a direct effect of the newly synthesized inhibitors on CRM1, rather than on off-targets. Crystal structures of CRM1 bound to KPT-276 or to previously reported inhibitors (KPT-185 and KPT-251) further showed specificity of the difluoroazetidinepropenonenyl group for the catalytic binding pocket of the CRM1 protein **(Supplementary Fig. 1d-i)**. To begin characterizing the potential of antagonizing CRM1 function for treating demyelinating disorders, we first characterized *Xpo1/Crm1* expression levels in multiple cell types in the central nervous system and in immune cells of the periphery (**Supplementary Fig. 2a-b**) which revealed a ubiquitous expression. Another important feature of CRM1 inhibitors was the low cytotoxicity in post-mitotic cells. Evaluation of survival using the MTT mitochondrial reductase activity assay in cultured neurons derived from the spinal cord or cortex, in mature oligodendrocytes, astrocytes, or splenocytes did not reveal any toxicity at a concentration range between 0.1 and 1000 nM

(**Supplementary Fig. 2c-h**). The only exception was proliferating oligodendrocyte progenitor cells, which were sensitive to high dose of the compounds, far above the therapeutic range.

CRM1 inhibitors decrease the severity of EAE

To test the translational value of the newly synthesized CRM inhibitors, we first used a widely accepted preclinical model of demyelination, called experimental autoimmune encephalomyelitis (EAE), which shares many pathological hallmarks of MS, including immune cell activation and CNS infiltration, demyelination and axonal damage[23]. To ascertain the potential for therapeutic application of the CRM1 inhibitors we designed a double-blind experiment in which treatment started after mice developed hindlimb paralysis (EAE clinical score of 2.5), which on average occurred 16 days after immunization (**Fig. 3a; Supplementary video 1**). Mice were gavaged every other day either with vehicle, or with the CRM1 inhibitors KPT-276 (75 mg/kg) or KPT-350 (7.5 mg/kg) at doses that were consistent with their *in vitro* binding affinity and well below the maximum tolerated dose defined in toxicology studies (data not shown). No overt signs of toxicity were detected in the different treatment groups, as we did not detect increased mortality, or adverse effect on weight (**Supplementary Fig. 3a),** or body condition **(Supplementary Fig. 3b)** in the treated mice compared to controls. The therapeutic efficacy of CRM1 inhibitors was demonstrated by their ability to decrease clinical progression, in treated mice compared to vehicle-treated controls. While the vehicle treated mice progressed to full quadriplegia (**Supplementary video 2**), the motor signs of KPT-276 (**Supplementary video 3)** and KPT-350 (**Supplementary video 4)** treated mice, substantially improved over time, as reflected by the decrease in overall cumulative disease score in the KPT-276 (60% ± 4.72) and KPT-350 (75% ± 4.32) treated group (**Fig. 3b**). When toluidine blue sections were analyzed at drug start time, which corresponded to a clinical score of 2.5 in the EAE model, we observed limited areas of myelin damage (**Supplementary Fig.3c-d),** delineated by the presence of immune cell infiltrates (**Fig 3c**). Treatment of mice with the CRM1 inhibitors KPT-276 and KPT-350, largely preserved both myelinated and demyelinated axons in the lumbo-sacral area of the spinal cord (**Fig 3d**), and this was in sharp contrast with vehicle-treated controls, whose spinal cords were characterized by large areas of axonal destruction, as clearly detected by a three-dimensional serial electron microscopic analysis (**Fig 3d**).

To further determine whether the presence of higher number of myelinated fibers in mice treated with the CRM1 inhibitors could also be consequent to enhanced regenerative processes induced in oligodendrocyte lineage cells, we performed immunohistochemistry with antibodies specific NG2 to label progenitors and CC1 to label oligodendrocytes. We then quantified the number of progenitors and mature oligodendrocytes outside the lesion areas in KPT-276 and KPT-350 treated mice compared to controls and did not detect any significant change in cell numbers (**Fig. 3e**), or myelin gene transcripts (**Supplementary Fig. 4a**) and this was consistent with the similar number of remyelinated axons counted in semithin spinal cord sections from mice treated with CRM1 inhibitors compared to vehicle controls (**Fig 3f**). To further evaluate cell-specific direct effects of CRM1 inhibitors on oligodendrocyte lineage cells, we treated cultured oligodendrocytes with the compounds and assessed proliferation (**Supplementary Fig. 4d**) and differentiation (**Supplementary Fig.**

4b-c) using immunocytochemistry, which did not reveal any statistically significant difference between treatment and control groups. These data suggest that the effect of CRM1 inhibitors in EAE could not be attributed to a direct effect on oligodendrocyte lineage cells.

CRM1 inhibitors reduce the inflammatory burden of the CNS

To define the mechanisms underlying the positive effect of the compounds in preventing clinical progression in EAE, we stained the lumbosacral cord with hematoxylin and eosin. The start point of treatment was characterized by the presence of several inflammatory infiltrates in the spinal cord (**Fig. 4a**). Analysis after 12 days of treatment revealed significantly fewer inflammatory lesions in the lumbosacral spinal cord of mice treated with the CRM1 inhibitors compared to controls (**Fig. 4b**). FACS analysis of immune cells from the spinal cord at the end of treatment (**Fig. 4c)** confirmed a reduction in the numbers of CD45+ leukocytes (*$p < 0.05$ for KPT-276, **$p < 0.01$ for KPT-350), B220+ B cells (*$p < 0.05$), and CD4+ and CD8+ T cells (*$p < 0.05$ for KPT-276, **$p < 0.01$ for KPT-350) in treated mice compared to vehicle controls (**Fig. 4d)**. This number was also lower than that at treatment start (**Fig. 4d)**. Microglial cells were also reduced in treated mice compared to controls **(Fig. 4d-f)**. The reduced inflammatory burden in the CNS resulted in decreased cytokine messenger RNA levels (*Il6, Tgfb1, Il10, Il17a, Tnf, Ifng*) (**Fig. 4g**). Treatment with CRM1 inhibitors also affected the peripheral immune system (**Fig. 4h**), as shown by the overall decrease of total splenocytes (**Supplementary Fig. 5a-b**), and of B, T cells, monocytes, neutrophils and dendritic cell populations (**Fig. 4h and Supplementary Fig. 5c)**. However, treatment with CRM1 inhibitors did not impair the ability of splenocytes to express cytokines (**Fig. 4i),** as shown by the ability of splenocytes acutely isolated from treated mice, to make IFNγ and IL17a (**Fig. 4j**). Thus, immune cells remained functional after CRM1 inhibition, and the overall decrease of distinct cell populations in the spleen and spinal cord was the consequence of decreased proliferation **(Fig. 4k)**, associated with a four fold increase (***$p = 0.0003$, data not shown) in nuclear accumulation of cell cycle inhibitory molecules (e.g. p27Kip1) (**Fig. 4l**) and possibly by the induction of p21 mediated cell cycle arrest [24]. Thus, the immunomodulatory effect of the CRM1 inhibitors was mediated by an effect on cell proliferation rather than a toxic effect on immune cells. To confirm lack of cytotoxicity, we performed a washout experiment of CRM1 inhibitors in naïve mice and detected a recovery of the number of splenocytes (**Supplementary Fig. 6a-b**), thereby supporting the reversibility of CRM1 inhibition and the safety of treatment with the novel compounds. To further demonstrate the immunomodulatory role of the CRM1 inhibitors we tested whether prophylactic treatment of EAE mice at time of immunization, would prevent disease onset. In agreement with the predicted outcome, both disease onset and severity (**Supplementary Fig. 7a-b**) were significantly decreased in treated mice compared to controls. No significant impact was observed on mouse weight **(Supplementary Fig. 7c)** or body condition **(Supplementary Fig. 7d)**, and immunophenotypic profiling of the spinal cord of treated mice revealed a reduction of B220+ B cells, CD4+ and CD8+ T cells without altered microglia or monocyte numbers (**Supplementary Fig. 7e**). Also in this paradigm we detected an effect of treatment on the total number of splenocytes (**Supplementary Fig. 7f**) and reductions in splenic cell

populations (**Supplementary Fig. 7g**). Together, these data suggest that CRM1 inhibitors have a non-toxic reversible effect on immune cell number in the periphery.

CRM1 inhibitor treatment preserves axonal integrity

In addition to the immunomodulatory role of CRM1 inhibitors, we asked whether the block of clinical progression after treatment could also be attributed to a direct neuroprotective effect. At treatment start point, when mice exhibited hindlimb paralysis, detectable but modest axonal damage could be detected in association with inflammatory infiltrates (**Fig. 5a-b**). After 12 days however, spinal cord sections from vehicle treated control mice were characterized by extensive axonal damage while sections from mice treated with CRM1 inhibitors displayed the same levels of damage as at start time point (**Fig. 5a-b**). While massive areas of neuronal loss and severely damaged axons with extensive cytoskeletal disruption and localized enlargements were detected in vehicle-treated spinal cords (**Fig. 5c),** the cytoskeletal integrity and axonal diameter were well preserved in mice treated with CRM1 inhibitors, despite myelin loss or myelin damage (**Fig. 5c-f**). Quantification of these findings revealed fewer axons with Wallerian degeneration (**Fig. 5d**), and an overall preservation of axons per unit area in the lumbosacral spinal cord of treated mice (**Fig. 5e**). These morphological data were also supported by higher transcript levels of neurofilament heavy chain (*Nefh*) in treated mice compared to controls **(Supplementary Fig.8a**). Together, these results show a robust effect of KPT-350 treatment in preserving axonal integrity regardless of the presence or absence of myelin, thereby suggesting a direct neuroprotective effect of CRM1 inhibitor treatment. We therefore asked whether CRM1 inhibitors could be protective also in other models of direct axonal damage, independent of immune cell activation. We selected a model of axonal damage consequent to excito-toxicity and injected mice with kainic acid, a non-degradable analog of glutamate that induces excitotoxic death of pyramidal neurons in the CA3 region of the hippocampus[25]. Subcutaneous administration of kainic acid (2 mg/kg) was associated with the detection of axonal damage in the CA3 hippocampal region of control mice, but not in mice that were treated with CRM1 inhibitors (**Fig. 5g-h**). To further ascertain that the protective effect of CRM1 inhibitor treatment resulted from a direct action in neuronal cells rather than a potential modulation of microglial numbers in the kainic acid injection model, we also stained sections for microglial markers which revealed a similar number of cells (**Fig 5i-j**). Direct neuroprotection was then assessed in hippocampal slice cultures, which preserve the cytoarchitecture of the hippocampus in a dish. Treatment of slice cultures with kainic acid (5 μM) for 18h resulted in extensive axonal damage in the CA3 region that was clearly detected by SMI-32 immunoreactivity **(Supplementary Fig. 9a).** The same experiment conducted in the presence of CRM1 inhibitors, however resulted in significant axonal protection and reduced SMI-32 immunoreactivity **(Supplementary Fig. 9b)**. Thus CRM1 inhibitors act as broad neuroprotective agents and prevent also axonal damage induced by excitotoxicity.

In order to more carefully evaluate the effect of CRM1 inhibitors on mouse locomotion, we adopted a model of localized inflammatory demyelination targeting the dorsal column of the thoracic spinal cord and monitored hind paw position and coordination in mice using the Basso Motor Scale[26]. Briefly, mice were sensitized to MOG_{35-55} and localized demyelinated lesions in the dorsal columns were obtained by local injection of TNFα and IFNγ in the

thoracic spinal cord by adapting published procedures[27,28]. This paradigm induced a steady decline in motor function which could be quantified. To test the effectiveness of CRM1 inhibition in this model, mice were administered either vehicle or KPT-350 (7.5 mg/kg) when they displayed a BMS score of 5, which was characterized by lack of coordination of the hindlimbs and external rotation of the hind paws. Daily monitoring in an open field platform was performed in a double-blinded fashion. While vehicle-treated mice progressed to almost full disability, KPT-350-treated mice stopped the progression of the motor dysfunction and partially recovered motor movement (**Fig 6a**), as indicated by statistically significant differences in the cumulative BMS score (**Fig. 6b**). The improved motor function was not associated with any detectable changes in the level of FluoroMyelin staining (**Fig. 6c-d**), but with clear differences in the number of damaged axons (**Fig 6e-f**) and microglial numbers (**Fig 6g-h**). Thus, also in a localized model of inflammatory demyelination, CRM1 inhibitors were effective in preventing clinical disease progression and retaining motor function.

Viral knockdown of Xpo1/Crm1 protects from axonal damage

To further evaluate the direct neuroprotective effect of CRM1 inhibition we also used cultured neurons treated with cytokine and excitatory aminoacids to induce focal axonal damage, as revealed by the presence of localized swellings co-stained with neurofilament H and the antibody SMI-32, which recognizes damaged axons (**Fig. 7a**). A statistically significant reduction in the number of damaged neuronal processes was detected in KPT-350 ($x = 79\%, \pm 1.09, n = 60$; $^{***}p < 0.001$) treated cultures compared to controls (**Fig. 7b**). Viral knockdown of *Xpo1*, the gene encoding for CRM1 (**Fig 7c**) was obtained by using lentiviral vectors, which reduced the relative nuclear CRM1 intensity to 36% ± 3 of the control value ($^{**}p = 0.0034$, data not shown). The SMI-32 immunoreactivity in cultures with reduced CRM1 levels was also reduced to 36% ± 16 ($^{*}p = 0.0231$, data not shown) of the neuronal cultures exposed to the excito-toxin. These results suggested that reduction of CRM1 was capable of protecting neurons from kainic acid-induced excito-toxic damage (**Fig. 7c).** The similarity of the neuroprotective effect of pharmacological inhibition and viral knockdown of *Xpo1* in neurons further supported a direct neuroprotective role of CRM1 inhibition.

Additional support for the protective effect of CRM1 inhibitor treatment on axonal damage was the evidence of rescued mitochondrial motility in models of neurotoxicity, as shown by live microscopy of fluorescently labeled mitochondria using MitoTracker® Green FM dye (**Fig. 7d**). Treatment of neurons with glutamate and TNFα significantly reduced mitochondrial speed from 7.2 ± 1.6 μm/sec to 3.0 ± 0.6 μm/sec ($^{*}p < 0.05$) (**Fig. 7e**), an effect associated also with decreased mitochondrial length (**Fig. 7f**) and both events were blocked by treatment with the CRM1 inhibitor KPT-350 ($p > 0.05$ vs. control). Because altered mitochondrial dynamics is often associated with impaired function, we also measured the oxygen consumption rate using the Seahorse Bioanalyzer in neurons treated with glutamate and TNFα in the presence or absence of CRM1 inhibitors. Glutamate and TNFα treatment induced a reduction of neuronal mitochondria spare respiratory capacity ($x = 24\% \pm 4.14$; $n = 12$ cultures; $^{*}p < 0.05$ vs. control), which was not detected in neurons treated with the CRM1 inhibitors **(Supplementary Fig. 10a-b**). Since decreased

mitochondrial function is hallmark of axonal damage in MS, these data further support the importance of CRM1 inhibitors as therapeutic agents preventing clinical progression.

Molecular targets of CRM1 inhibition in vitro and in vivo

To define the molecular mechanism underlying the neuroprotective effect of KPT350 in cultured neurons we adopted a mass-spectrometry analysis of molecules with cytosolic accumulation in neurons treated with glutamate and TNFα in the absence of the KPT compound but not in its presence (**Fig. 8a**). We reasoned that these molecules must be targets of CRM1 nuclear export in pathological conditions and they also contained nuclear export signals. Among the identified molecules we detected: TAU and amyloid precursor protein, which have been associated with Alzheimer's disease, FUS and TDP-43 associated with axonal damage in ALS and NRF2, a transcription factor modulating the expression of genes involved in the response to oxidative stress in several pathologies, including MS[17]. To further validate the subcellular localization of these molecules in our experimental system, we performed western blots of cytosolic and nuclear fractions prepared from cultured neurons exposed to glutamate and TNFα with and without KPT-350 (**Fig. 8b**). Immunoblot analysis confirmed the nuclear retention of TAU and NRF2, in protected neurons (**Fig. 8c**)[17,18].

Similar results were also detected in vivo, in the spinal cords of vehicle and KPT-350-treated mice **(Fig. 8d)**. These experiments further supported the nuclear retention of TAU and NRF2 in neurons in the spinal cord of KPT-treated mice (**Fig. 8e**) compared to controls, a finding which was also confirmed by immunohistochemistry (**Fig. 8f**). The number of NeuN+ neurons with nuclear NRF2 was significantly increased in KPT-350 treated spinal cords compared to controls (**$p < 0.01$ vs. vehicle) (**Fig. 8g**). The transcript levels of NRF2 target genes such as *Nqo1* (nicotinamide adenine dinucleotide phosphate dehydrogenase (quinone 1), encoding a protein involved in detoxification of cytotoxic quinones, and *Gclc* (glutamate-cysteine ligase catalytic subunit), encoding an enzyme involved in the biosynthesis of glutathione, were also increased in the KPT-treated mice (**Fig. 8h**), thereby suggesting an overall enhancement of the antioxidant response.

Combined, these data suggest that CRM1 inhibitors halt clinical disease progression in preclinical models of demyelination by a dual mechanism that targets both immune cell function and neuroprotection.

DISCUSSION

Aberrant nuclear export has been reported in a large number of pathologies associated with axonal damage, including traumatic brain injury[29], Alzheimer's disease[30], amyotrophic lateral sclerosis (ALS)[6,31,32] and multiple sclerosis (MS)[4]. We have previously proposed that cytoplasmic localization of molecules that in physiological conditions are localized in the nucleus, results in aberrant function and axonal damage in MS[33]. However nucleo-cytoplasmic shuttling is impaired in several neurodegenerative diseases characterized by axonal damage. For instance, in Alzheimer's disease, the nuclear export of cell cycle inhibitors in neurons has been implicated in aberrant cell cycle re-entry (reviewed in[34]). Export of TAU, a microtubule binding protein has been associated with axonal damage

when accumulated in the cytoplasm, and to exert a neuroprotective function when localized in the nucleus[35,36]. In MS brains and in models of axonal damage associated with exposure to cytokines and excitotoxins, nuclear export of HDAC1 into the axoplasm has been shown to interfere with mitochondrial movement, by a mechanism of sequestration of motor proteins[4]. Nuclear localization of the transcription factor NRF2 (nuclear factor (erythroid-derived 2)-like 2), has been shown to be critically important for responsible for transcription of genes involved in anti-oxidant defense and its activation is neuroprotective. Nuclear export of NRF2 in cerebellar neurons, has been associated with impaired response to oxidative stress[15-18]. Taken together, these studies suggested that neurodegeneration and axonal damage correlated with mis-localization of nuclear molecules to the cytoplasm while protection was favored by their retention in the nuclear compartment, and led to the hypothesis that nuclear exportin could be effective targets to reduce axonal damage.

Nuclear export is a highly regulated cellular function mediated by two large family of proteins: the importins (16 family members), involved in the transport from the cytosol to the nucleus of cells and the exportins (6 family members) which are responsible for the selective export of molecules from the nucleus to the cytosol[37,38]. The exportin family includes several members, with distinct recognition domains and substrate specificity. Among the family members, CRM1, which recognizes leucine-rich motifs in proteins, has been associated with the occurrence of axonal damage[4,29]. This molecule is up-regulated in models of traumatic brain injury and in this study we report its up-regulation in neurons within MS lesions, which is consistent with aberrant nuclear export detected in these conditions. Furthermore, CRM1 – dependent transport has been shown to modulate subcellular localization of NRF2[18]. This study also identifies nuclear retention of NRF2 and TAU in neurons as neuroprotective mechanisms associated with CRM1 inhibition. We report here the pre-clinical efficacy of a novel class of pharmacological compounds targeting CRM1 in three distinct animal models: MOG-induced EAE, localized inflammatory demyelination of dorsal columns in the spinal cord and a mouse model of excitotoxicity induced by kainate injection.

Neuroprotection consequent to CRM1-mediated inhibition axonal damage was associated with a dual targeting of immune and neuronal cells. In neurons, inhibition of CRM1 mediated nuclear export resulted in improved mitochondrial transport and function possibly resulting from nuclear retention of “axono-toxic” molecules (e.g. TAU), and consequent preservation of cytoskeletal integrity. Inhibition of nuclear export also favored accumulation of “protective” molecule such as transcription factors involved in modulation of the anti-oxidant response (e.g. NRF2), thereby increasing the protective response of neurons to oxidative stress. In immune cells, CRM1 inhibitors decreased proliferation of immune cells by favoring nuclear accumulation of molecules involved in cell cycle arrest and thereby decreasing the inflammatory burden[21]. Treatment was not cytotoxic on immune cells, as their number was rapidly restored upon washout of the drug and immune cells retained the ability to produce cytokines. Thus, inhibition of CRM1-mediated nuclear export favored neuroprotection by acting both, on neuroinflammation and on axonal transport disruption and neuronal defense against oxidative stress.

Several studies have focused on potential causes of axonal damage in multiple sclerosis that are caused by mechanisms independent of peripheral immune cell infiltration and the subsequent cytotoxicity that is characteristic of inflammatory demyelination[39]. These other signals, which are also shared with several neurodegenerative diseases, include resident microglia activation[40], energetic failure of neurons due to mitochondrial functional impairment[41], and mitochondrial fragmentation/movement defects[3] and the accumulation in the cytoplasm of nuclear proteins. Our data indicate that KPT compounds provide neuroprotection by targeting multiple causes of axonal damage. The KPT inhibitors protected axons by directly targeting neuronal CRM1 and indirectly by reducing inflammation.

Many of the current available therapies for MS target either peripheral immune cell function[42], or their ability to cross into the brain parenchyma, however, these compounds have not been able to stop the progression of axonal damage despite immunomodulatory intervention[43]. Advancing other therapies that target also other components of MS pathophysiology has proven to be more challenging. For example, targeting microglial activation has been shown to have both detrimental and beneficial roles in axonal physiology[44]. Remyelination strategies have been recently proposed as providing neuroprotective effects on myelinated axons. Our study provides a novel approach that is both immunomodulatory and neuroprotective. The eventual combination with remyelination therapies, and/or symptomatic therapies may prove useful to address the current multiple therapeutic needs of multiple sclerosis patients. CRM1 inhibitors are also orally bioavailable and cross the blood brain barrier, and additional safety and efficacy studies will be needed to test its utility for patients who require long-term therapy options.

METHODS

Animals

All animal experiments were approved by the Icahn School of Medicine at Mount Sinai Animal Care Committee. All mice were obtained from Jackson Laboratories, and rats from Charles River Laboratories. Mice were housed at a maximum of five animals per cage. Rats were housed as a single pregnant female per cage. All animals were exposed to a normal 12 hr light-dark cycle, and provided *ad libitum* with food and water.

Reagents and supplies

All reagents and supplies were from Fisher Scientific or Sigma-Aldrich. Karyopharm Therapeutics Inc. supplied the *in vitro* and *in vivo* formulations of KPT-276, and KPT-350, and the vehicle control compounds, Pluronic® F-68 and PVP K-29/32.

Structural determination of KPT-276 bound CRM1

Crystal structure determination is as previously described[20-22,45]. Briefly, ^{Sc}CRM1 (Thr539 mutated to cysteine to allow inhibitor binding; residues 377–413 and 1059–1084 removed to improve crystal quality), human Ran and *S. cerevisiae* RanBP1 (residues 1–61 removed to improve crystal quality) were expressed and purified separately and then assembled to form a ternary complex. The CRM1-Ran-RanBP1 complex was mixed with KPT-276 at 1:5 ratio

and further purified by size exclusion chromatography followed by crystallization and structure determination. Figures showing the structures were prepared using Pymol (DeLano Scientific LLB, Palo Alto, CA) and the omit electron density map was generated using CCP4[46].

In vitro GST pull-down inhibition assay

10 μM of purified recombinant *Hs*CRM1 was incubated with or without 100 μM KPT-276 in buffer containing 10 mM Tris pH 7.5, 100 mM sodium chloride, and 5 mM magnesium acetate, in a total volume of 100 μL. ~15 μg of GST or recombinant GST-NES (NES is residues 33–50 of the protein kinase-A inhibitor (PKIα)) immobilized on glutathione sepharose beads, and molar excess of RanGTP, were added to the CRM1 proteins and rotated for 30 min at 4°C. The glutathione sepharose beads were then washed extensively with 20 mM HEPES pH 7.5, 110 mM potassium acetate, 2 mM magnesium acetate, 1 mM EGTA, and 15% glycerol. Bound proteins were separated by SDS-PAGE gel and stained with Coomassie dye.

Pharmacokinetic (PK) measurements

KPT-276 (2 mg/kg) and KPT-350 (3 mg/kg) was administered via oral gavage in male Sprague-Dawley rats, with a mean body weight of approximately 210-230 g. At nine designated time points (1, 5, 15, 30 min and 1, 2, 4, 7 and 24 hr) post-gavage, the animals were restrained, and approximately 150 μL blood/time point was collected via the tail vein into pre-cooled K2EDTA tubes. Blood samples were placed on ice and centrifuged (2000g, 5 min at 4°C) to obtain plasma within 30 min of sample collection. After the blood collection, the animals were euthanized by pure CO_2 inhalation and the brain tissue was harvested. The whole brain was collected, rinsed with cold saline, dried on filtrate paper, weighed and then snap frozen by placing into dry-ice. All samples were stored at −80°C until further analysis. The PK parameters were determined by a non-compartmental module of WinNonlin Professional 6.2.

Experimental autoimmune encephalomyelitis (EAE)

EAE was performed as previously we have previously described[47]. Briefly, 8 week old female C57BL/6J mice (Jackson Laboratories) were immunized with 300 μg of murine myelin oligodendrocyte glycoprotein, peptide sequence 35–55 (MOG_{35-55}) in complete Freund's adjuvant (10 mL of incomplete Freund's adjuvant containing 500 μg of *Mycobacterium tuberculosis*). Mice were injected with 200 μL of a solution consisting of equal amounts of 1.5 mg/mL $MOG_{35–55}$ peptide, 2.5 mg/mL *Mycobacterium tuberculosis* and 50% Incomplete Freund's Adjuvant. On day 0 and day 2 the mice are injected intraperitoneally with 500 ng pertussis toxin (from *Bordetella pertussis*) in 200 μL PBS. The MOG_{35-55}/CFA injection was repeated on the opposite hind limb after seven days to boost the immunological reaction. Mice were monitored daily for clinical score based on a five-point scale, where 0 represents no disability a score of 1 corresponds to a flaccid tail, 2 is weak hind legs, 3 is hindlimb paralysis, 4 is quadriplegia and a score of 5 is death. Mice were also assessed for body condition (score BC1 - BC5, where BC3 represents a healthy body coat and weight; BC5 represents an obese mouse; BC1 is an anorexic mouse), and

weighed daily. At the onset of disability, the mice were provided *ad libitum* with water-moistened food that was supplemented with flavored gelatin. In addition, Nutrical® was provided as a high calorie supplement in order to prevent weight loss. Any mice that did not develop clinical symptoms (score 0) were excluded prior to the start of treatment. All other mice were assigned to treatment groups in a random manner, and scored and drug-treated in double-blinded fashion. Any mice that did not develop symptoms of EAE were not used in the treatment groups. All treatment groups were only revealed at the end of the experiments to ensure experimenter bias was not introduced. All measurements were taken in the vivarium during the light cycle.

Localized EAE to dorsal column of the spinal cord and mouse locomotion testing

Focal EAE was performed according to a modified protocol of Merkler D, et al.[27] and Chaudhary, P, et al.[28] Eight week old female C57BL/6J mice (Jackson Laboratories) were sensitized with a single dose of 300 μg of murine myelin oligodendrocyte glycoprotein emulsified in complete Freund's adjuvant (as described above). Seven days later, mice were anesthetized with ketamine and xylazine and a hemi-laminectomy was performed at thoracic level T5, and the spinal cord was stereotactically injected into the dorsal column of the spinal cord over a three minute period with a 1 μL cytokine mixture containing 250 ng recombinant mouse TNFα 250 (R&D Systems), and 150 U of recombinant mouse interferon-γ (R&D Systems). Mice were monitored daily for motor symptoms. Motor function was evaluated by hind-limb locomotor performance using the open-field Basso Mouse Scale (BMS)[26]. The scale consists of a non-linear scoring scale ranging from 0 (complete paralysis) to 9 (normal mobility), with each score represents a distinct motor functional state. Focal EAE mice were randomly assigned to treatment groups (either vehicle or KPT-350) starting at a BMS score of 5. Locomotor activity was assessed daily in an open field for 4 min and each mouse was assessed by two individual investigators that were blinded to the treatment groups. The treatment groups were only revealed at the completion of the experiment.

Kainic acid induced neurotoxicity ex vivo and in vivo

Organotypic slice cultures—Hippocampal slice cultures were prepared using the interface culture method[48] adapted for 5-7 day old C57/BL6J male mouse pups. Briefly, hippocampi were dissected under sterile conditions and sliced transversely at 400 μm with a McIlwain tissue chopper. Slices were plated on porous (0.4 μm) insert membranes (Millipore, Bedford, MA) and maintained at 37°C in a 5 % CO_2 incubator. Culture medium was changed every 2-3 days and experiments were performed after at least two weeks in culture. For inducing excitotoxicity, slices were first treated with 10 nM KPT-350 for 1 hr, followed by 5 μM kainic acid for 18 hr.

Kainic acid induced neurotoxicity in vivo—In vivo kainic acid experiments were performed in 12 month old male C57/BL6J mice. Mice were given KPT-350 (7.5 mg/kg) for one day prior to the subcutaneous injection of 2 mg/kg kainic acid which was used to induce neuronal damage in the CA3 region of the hippocampus. Mice were closely monitored for symptoms of seizure. After 1 hr, all mice were intraperitoneally injected with 40 mg/kg of sodium pentobarbital to temporarily anesthetize the animals. After 18 hr mice were perfused

with 4% paraformaldehyde and the brains were post-fixed for 1 day in paraformaldehyde, followed by soaking in 30% sucrose and embedding in OCT. Hippocampal sections were stained to assess neuronal damage.

Drug preparation, dosing and administration—The vehicle solution was comprised of 0.6% w/v Pluronic® F-68 and 0.6% w/v PVP K-29/32 in water. The final concentration of drug given to mice was 75 mg/kg of KPT-276 and 7.5 mg/kg of KPT-350. The drugs and vehicle were dosed three times per week (Monday, Wednesday and Friday) via oral gavage. For therapeutic EAE, treatment was started at day 16, at the onset of hindlimb paralysis (EAE clinical score of 2.5), and animals were dosed for a 12 day time window, and harvested on day 28. For prophylactic EAE, drug administration was started at the same time as immunization with MOG_{35-55} and mice were treated for a total of 19 days.

Primary neuronal, and oligodendrocyte cultures—Primary neuronal cultures were prepared as previously described [5, 49]. Briefly, pregnant Sprague-Dawley rats, or pregnant C57/BL6J mice at gestational day 16 were sacrificed by carbon dioxide asphyxiation. Cortices and hippocampi from embryos were removed, dissociated into a single cell suspension using 0.05% trypsin and mechanical disruption, and plated in Neurobasal media supplemented with B27 supplement (Invitrogen), glutamine and penicillin/streptomycin. For immunocytochemistry, hippocampal neurons were plated at a density of 1.3×10^5 cells/ml on poly-D-lysine coated glass coverslips. Cortical neurons were plated at a density of 6.6×10^5 on 10 cm dishes for western blot experiments. At the third day of culture, neurons were treated with the anti-mitotic AraC in Neurobasal media, for 1 day and changed back to regular media without anti-mitotic. The media was subsequently changed every 3-4 days. Primary cultures consisted of highly pure (> 97%) neuronal population, with less than 3% detectable $GFAP^+$ astrocytes, $Iba1^+$ microglia or MBP^+ oligodendrocytes as assessed by immunocytochemistry, and they were used for all experiments at 14 days of culture. Oligodendrocyte progenitors were isolated from the cortex of postnatal day 1 rats and cultured according to a modified McCarthy and de Vellis procedure. The cells were grown in NM10 (high glucose DMEM supplemented with 10% fetal bovine serum), and cultured for one week at 37°C, 5% CO2. After one week, loosely attached microglia were removed by a low-speed shaking (210 rpm) for 20 min on a rotary platform shaker. Media was removed and discarded and replaced with fresh NM10. The flasks were shaken overnight for 18–20 hr at 220 rpm and cells were positively immunoselected on a Miltenyi MACS magnetic purification column using mouse anti-A2B5 antibody. Primary oligodendrocytes were plated on poly-D-lysine coated dishes at a density of 2000 cells per cm^2 and grown in oligodendrocyte chemically-defined media containing 100 μg/mL bovine transferrin, 5.0 μg/mL yeast recombinant insulin, 100 μg/mL bovine serum albumin fraction V, 1 mg/mL biotin, 0.628 mg/mL progesterone, 0.3804 mg/mL sodium selenite, 16.1 μg/mL putrescine. For cell expansion, chemically-defined media was supplemented with 20 ng/mL basic fibroblast growth factor and 10 ng/mL platelet-derived growth factor-AA and cells were allowed to proliferate for 48 hours prior to treatment. Oligodendrocyte progenitor cultures are 99%+ pure $PDGFR\alpha^+$ cultures, with less than 1% detectable $GFAP^+$ astrocytes, or $Iba1^+$ microglia, as detected by immunocytochemistry.

MitoTracking, mitochondrial velocity and length measurements—Neurons were plated on glass-bottomed live imaging chambers at a density of 1×10^5 cells/mL. Hippocampal 14 DIV neurons were loaded with MitoTracker® Green FM dye in phenol red-free Neurobasal media. Following the 30 minute loading period, the cells were washed twice with Neurobasal and pre-treated for an additional 30 min with either vehicle control (DMSO), or KPT-350 (10 nM). Cells were then treated with glutamate (50 μM) and TNFα (200 ng/mL) in Neurobasal media. The cells were live imaged at 37°C on a Zeiss Observer Z1 microscope equipped with a XL S heating module. Pictures were taken every 5 seconds for a total of 5 minutes over a time period of 2 hours. MitoTracker® tracings were performed using the MTrackJ function plug-in on ImageJ and data are plotted as mean velocity (μm/sec) ± SEM. Mitochondrial lengths were measured from the same set of still images using the Measure function on ImageJ.

Viral knockdowns of *Xpo1*

Mouse hippocampal neurons (10 DIV) were infected with lentiviral particles (multiplicity of infection = 5) containing shRNA for knockdown of *Xpo1* (pLKO.1-CMV-tGFP, cat no: TRCN0000446624, 5'-TGG-TGA-CTT-TGC-CCG-CTT-TGA-3') or TurboGFP control (pLKO.1-CMV-tGFP Empty Vector Control) in the presence of 4 μg/mL of hexamethrine bromide (Sigma). After two days, infected neurons were identified by GFP fluorescence on a live imaging microscope, and then cells were treated with 5 μM kainic acid for 2 h. Following kainic acid treatment, cells were fixed with 4% PFA, and stained with antibodies for CRM1 (1:200, Santa Cruz, cat no: sc-5595), NFH (1:400, Millipore, cat no: MAB5448), SMI-32 (1:5000, Millipore, cat no: NE1023). Axonal damage was assessed by quantifying the intensity of SMI-32 immunoreactivity and expressing it as a ratio to the expression of NFH.

SeaHorse bioenergetic analysis—Oxygen consumption rate (OCR) of cultured hippocampal neurons (17 DIV) was measured using Seahorse XF24 analyzer (Seahorse Bioscience, Billerica, MA, USA) following the manufacturer's instructions. Neurons were grown in the assay plates at 8.4×10^4 cells per well. One hour before the experiment, cells were treated with SINE (either 10 nM KPT-276 or KPT-350) at the indicated doses and 30 min following SINE treatment, glutamate (50 μM) and TNFα (200 ng/mL) were added to the culture media. Bioenergetic analysis was then performed by sequentially injecting 2 μM oligomycin, 4 μM carbonyl cyanide *p*-(trifluoromethoxy) phenylhydrazone (FCCP), 0.5 μM rotenone and 4 μM antimycin. Results from at least three independent experiments are shown and data are expressed as a percentage of the basal OCR in DMSO-treated cells.

MTT toxicity assays—Cells were plated in 48 well plates at a density of 25,000 cells/cm^2. For total splenocytes and GM-CSF induced, bone marrow derived dendritic cells, 10^6 cells were plated in 96 well plates. Both cortical and spinal cord neurons were treated with 0.1 to 1000 nM KPT-276 or KPT-350 for 24 hr and then MTT reagents was added for 4 hrs. The media was aspirated and the formazan crystals were solubilized in DMSO, and the solute was measured spectrophotometrically at 540 nm with background subtraction at 655 nm. Data were normalized as percent of control.

Protein extraction, cytosolic and nuclear fractionations, proteomics, SDS-PAGE and western blotting—Human post-mortem cortical gray matter from MS patients and controls was provided by the United Kingdom Brain Bank. A small piece gray matter was micro-dissected on a cold steel block under a stereomicroscope to ensure the sample was free of white matter or meningeal material. Tissue was lysed with RIPA lysis buffer in a Qiagen TissueLyser LT, and centrifuged at 15,000×g to obtain a post-nuclear supernatant for western blot analysis. For cytosolic and nuclear fractionation of cultured cells and mouse spinal cord tissue, a method employing a hypotonic-lysis buffer, followed by NP40 detergent isolation was used (ActiveMotif). Proteomics was performed on cytosolic fractions of cortical neurons, and on EAE spinal cords. Proteomics was performed on a Thermo Q-Exactive LC-MS/MS instrument. The data were filtered to include only the 1,573 gene products that had six or more spectra when considering the combined three replicates. Protein amounts were determined using the Bradford protein assay, and samples (25 μg/lane) were resolved by SDS-PAGE on pre-cast BioRad gels and transferred to PVDF membranes. Membranes were blocked in 5% (wt/vol) skim milk powder in TBS-tween (TBST) and incubated overnight with primary antibodies (CRM1, BD Transduction Labs, cat no: 611832, 1:1000; ACTIN clone AC-15, Sigma, cat no: A5541, 1:5000; MEK1/2, Sigma, cat no: M5795, 1:10,000; HISTONE H3, Abcam, cat no: AB1791, 1:5000; FUS, Abcam, cat no: EP1207Y, 1:250; total TAU, clone 86E/C11, Millipore, cat no: 05-803, 1:1000; NRF2, Santa Cruz, cat no: sc-722, 1:100) diluted in 5% bovine serum albumin in TBST. The next day, membranes were washed with TBST and incubated with secondary antibody diluted 1:25,000 (goat-anti-mouse-HRP, or goat-anti-rabbit-HRP, JacksonImmunoResearch) for 1 hr. Blots were incubated with Amersham ECL reagent, and imaged and quantified on a BioRad Molecular Imager ChemiDoc™ with Image Lab XRS+ Software.

RNA extraction and qPCR—An equal size weight (10 mg) piece of spleen or lumbar-sacral region of spinal cord region from therapeutically treated EAE mice harvested at d28 was dissected and flash frozen on dry ice for RNA extraction. RNA was extracted using Trizol (Invitrogen, #15596-018) and purified with the RNeasy Micro kit (Qiagen, #74004) following the manufacturer's protocol. The total RNA amount was quantified on nanodrop, and 1 μg of total RNA was reverse transcribed with qScript cDNA Supermix (Quanta, #95048) and qRT-PCR was performed using Perfecta Sybr Fast Mix Rox 1250 (Quanta, #101414-278) (primers are listed in **Table 3).** After normalization to *18S rRNA*, the average values for each transcript was calculated based on the values obtained in all the samples included for each experimental condition. Transcripts levels were normalized based on calculated primer efficiencies.

Immunocytochemistry, immunohistochemistry and quantitative confocal microscopy—Following experimental treatments, cells were washed once with 1x PBS and fixed with 4% (wt/vol) paraformaldehyde. Cells were permeabilized with blocking buffer (0.1 M phosphate buffer (PB), 10% (vol/vol) normal goat serum (Vector Laboratories) and 0.5% (vol/vol) Triton X-100) and incubated with primary antibodies (NFH, Millipore, cat no: MAB5448, 1:400; SMI-32, Millipore, cat no: NE1023, 1:5000; OLIG2, Chemicon, cat no: AB9610, 1:500; activated CASPASE-3, Abcam, ab13847, 1:100)

overnight and then washed 3 × 5 min with PB and incubated with the primary antibody overnight. Coverslips were washed 3 × 5 min with PB and incubated with secondary antibodies (goat-anti-rabbit-Alexa^{488}, or – Alexa^{594}, Invitrogen, diluted 1:500 in blocking buffer). Cellular nuclei were counterstained with DAPI (0.1 μg/mL) for 5 min prior to mounting. For immunohistochemistry, mice were anaesthetized and perfused with 4% (wt/vol) paraformaldehyde. Spinal cords were removed, post-fixed, and cryopreserved in 30% (wt/vol) sucrose, embedded in OCT and sectioned longitudinally (8 μm). Spinal cord sections were permeabilized with blocking buffer (0.1 M phosphate buffer (PB), 10% (vol/vol) normal goat serum (Vector Laboratories) and 0.5% (vol/vol) Triton X-100) and incubated with stains (FluoroMyelin, Invitrogen 1:300) or primary antibodies (CC1/APC, Calbiochem, cat no: OP80, 1:200; MBP, Millipore, cat no: MAB386, 1:400; NG2, Millipore, cat no: 24447, 1:250; IBA1, Wako, cat no: 019-19741) overnight and then washed 3 × 5 min with PB and incubated with the primary antibody overnight, and incubated with corresponding secondary antibodies, followed by counterstaining with DAPI (as above).

For human tissue lesional and non-lesional areas of paraformaldehyde fixed, paraffin embedded human brain biopsies were sectioned and antigen retrieval was performed using a microwave or a steamer and sodium citrate buffer, pH 6.0. Slides were incubated overnight with antibodies for anti-MBP (Dako, cat no: 1: 1000), anti-neurofilament (Dako, 1:2000), anti-CD45 (Dako, 1:800), anti-CRM1 (Santa Cruz, cat no: sc-5595, 1:100), anti-NeuN (Chemicon, cat no: MAB377, 1:100). To identify blood derived monocytes, microglia and their activated derivatives we used the antibody KiM1P (1: 5000 (kindly provided by H.-J. Radzun, Department of Pathology, University of Göttingen, Germany)). This antibody recognizes the antigen CD68 and has been especially designed to label all CD68-positive cells in paraffin embedded human tissue samples including monocytes, ramified microglia and foamy phagocytes. Secondary antibodies were biotinylated anti-rabbit (Vector Laboratories, 1:400) or anti-mouse (GE Healthcare, 1:400) antibodies followed by ExtrAvidin-Peroxidase (1: 100; Sigma). DAB was used as a chromogen and sections were counterstained using hematoxylin. For double staining, sections were incubated with Cy3 (Jackson ImmunoResearch, 1:200) or Alexa488 (Jackson ImmunoResearch, 1:200) conjugated antibodies and counterstained with DAPI (Invitrogen, 1:5000). All images were taken on a Zeiss LSM-710 confocal microscope with Zen software or an Olympus fluorescent microscope. Axonal damage was assessed by either assessing neuritic beading, which was defined as neurites exhibiting a non-smooth morphology, characterized by a pattern of successive swellings/enlargements, and/or severed neurites. A second measure of axonal damage was obtained by expressing the ratio of SMI-32 to NFH immunoreactivity, which was quantified using ImageJ.

Hematoxylin and eosin staining—EAE mice were perfused at d28 and spinal cords were removed, soaked in 30% sucrose solution in PBS (wt/vol), embedded in OCT and frozen on dry ice. Ten micron thick frozen sections were cut on a cryostat, and washed twice in xylene, with subsequent washes in 100%, and 95% ethanol for three minutes each. Following this, the slides are washed in water, and placed in hematoxylin solution for three minutes. The slides are then washed with water, and acidified alcohol (95% alcohol + 5%

glacial acetic acid), followed by washing in 5% ammonium hydroxide. The slides are incubated in eosin solution, followed by dehydration again in ethanol (100% and 95%), with a final wash in xylene before mounting with a coverslip.

Serial electron microscopy—For serially-reconstructed electron microscopy, animals (n = 3 per group) were rapidly perfused with 4% paraformaldehyde, 2.5% glutaraldehyde in sodium cacodylate buffer, pH 7.2. Spinal columns were removed and spinal cords were processed in L4-L5 region with embedded in Epon plastic. Semithin sections (1 mm) were stained for myelin with 1% toluidine blue/1% sodium borate. Following identification of an appropriate region for EM analysis, tissue was embedded and cut into semi-thin sections for three-dimensional electron microscopy (Renovo Inc, Cleveland, OH). For ultrastructural imaging, a SigmaVP microscope from Zeiss was used with a 3 view door from Gatan. A low kv backscatter detector (Gatan) was used to detect the signal. For cytoskeletal analysis, 200 axons were analyzed, and scored based on the percent microtubules either intact, or with varying degrees of disruption.

Proliferation of CD4 T cells—$CD4^+$ cells were negatively selected from total splenocytes by use of a cocktail of antibody-coated magnetic beads from Miltenyi Biotech (CD8a, CD11b, CD11c, CD19, CD45R (B220), CD49b (DX5), CD105, Anti-MHC-class II, and Ter-119), according to manufacturer's instructions. CD4+ T cells were labeled with carboxyfluorescein diacetate succinimidyl ester (CFSE) (Life Technologies Inc.) and cultured at 1×10^5cells/well for 48 hours in anti-CD3 (BD) and anti-CD28 (BD) coated microplates (5 μg/mL) with or without mouse rIL2 (BD) (10 ng/mL). Cells were cultured in RPMI-1640 supplemented with Glutamax, 10% fetal calf serum, 0.02 mM 2β-mercaptoethanol, and antibiotics. CFSE dilution analyzed by flow cytometry was used to determine the percentage of proliferating CD4+.

FACS analysis—Mice were euthanized using CO_2 and the spleen and spinal cord were immediately removed and placed into cold PBS. The tissue was dissociated with a 40 micron filter and centrifuged to obtain a single cell suspension. APC-conjugated anti-CD45R (B220; RA3-6B2), anti–IFN-γ (XMG1.2), anti-MHCII (AF6-1201), PE-conjugated, anti–IL-17A (TC11-18H10) were from BD. Efluor450-conjugated anti-CD11b (M1/70), CD8α (53-6.1), APC-conjugated anti-CD115 (AFS98), PE-Cy7–conjugated anti-CD11c (N418), anti-CD4 (GK1.5), Alexa fluor 700-conjugated CD45 (30-F11), PercPCy5.5-conjugated CD3ε (145-2C11) were from eBioscience. For intracellular cytokine staining, lymphocytes were stimulated *in vitro* with leukocyte activation cocktail (BD) according to the manufacturer's instructions. Surface staining was performed before permeabilization using an intracellular staining kit (eBioscience). For staining of spinal cord cells, spinal columns were flushed with cold PBS, and the cord was mashed through a cell strainer. Mononuclear cells were separated by density gradient centrifugation on Percoll (GE Healthcare). Forward scatter and side scatter were used to gate cells excluding debris and cell aggregates and 7-AAD (BioLegend) was used to gate out dead cells. Samples were analyzed using a flow cytometer (LSRFortessa; BD) and the resulting data were analyzed using FlowJo software (Tree Star, Inc).

Relative spleen cell population calculations—The populations analyzed by FACS in the spleen (B220+ cells, CD4+ cells, CD8+ cells, monocytes, neutrophils and dendritic cells) represent approximately 90% of spleen cellularity when erythrocytes are excluded. In order to represent relative spleen cell populations in pie graph format, the sum of these leukocyte numbers was considered to be 100% of total cells.

NES prediction—NES predictions were performed using NetNES 1.1 server (http://www.cbs.dtu.dk/services/NetNES/). Mouse protein accession numbers were accessed through the National Library of Medicine, and the primary amino acid sequence was queried for containing leucine-rich sequences indicative of an NES[50].

Sample size, data analysis and statistics—All data were analyzed using GraphPad Prism 5.0 software. All data represents means ± standard error of the mean (SEM). All statistical tests were two-tailed, and performed using parametric statistics (independent t-tests with Bonferroni correction, one-way ANOVA with Dunnett's correction, or linear regression analysis) when data were normally distributed (tested using GraphPad), and the assumptions underlying the given tests were met. Non-parametric equivalent statistical tests (e.g., Mann-Whitney U tests, or Kruskal-Wallis tests with Dunn's correction) were used when data were not normally distributed, or when variances were largely different between groups. No statistical methods were used to pre-determine sample sizes, but our samples sizes are similar or higher than those employed in the field. Human sample sizes were limited, and thus we used the number of samples we had access to. All data were considered significant at $p < 0.05$.

A supplementary methods checklist is available.

Supplementary Material

Refer to Web version on PubMed Central for supplementary material.

Acknowledgements

We thank Mr. Thomas Flagiello and Ms. Xiomara Pedre for assistance with EAE animal experiments. **Funding:** The project was supported by NIH grants R01-NS69385, R37-NS42925 and from seed funds from Karyopharm Therapeutics to PC, and from the Fast Forward, LLC, division of the National Multiple Sclerosis Society to PC and SS. TK was supported by funds from the Interdisciplinary Centre for Clinical Research in Münster (KuT3/006/11). OH is the recipient of the Mount Sinai Helmsley Award. JDH holds a postdoctoral fellowship from the Multiple Sclerosis Society of Canada and the Fonds de la recherche en santé du Québec. Human tissue samples for western blotting were supplied by the UK Multiple Sclerosis Tissue Bank funded by the MS Society of Great Britain and Northern Ireland, registered charity 207495.

REFERENCES

1. Trapp BD, et al. Axonal transection in the lesions of multiple sclerosis. The New England journal of medicine. 1998; 338:278–285. [PubMed: 9445407]
2. Ferguson B, Matyszak MK, Esiri MM, Perry VH. Axonal damage in acute multiple sclerosis lesions. Brain : a journal of neurology. 1997; 120(Pt 3):393–399. [PubMed: 9126051]
3. Nikic I, et al. A reversible form of axon damage in experimental autoimmune encephalomyelitis and multiple sclerosis. Nature medicine. 2011; 17:495–499.

4. Kim JY, et al. HDAC1 nuclear export induced by pathological conditions is essential for the onset of axonal damage. Nature neuroscience. 2010; 13:180–189. [PubMed: 20037577]
5. Dormann D, et al. ALS-associated fused in sarcoma (FUS) mutations disrupt Transportin-mediated nuclear import. The EMBO journal. 2010; 29:2841–2857. [PubMed: 20606625]
6. Zhang ZC, Chook YM. Structural and energetic basis of ALS-causing mutations in the atypical prolinetyrosine nuclear localization signal of the Fused in Sarcoma protein (FUS). Proceedings of the National Academy of Sciences of the United States of America. 2012; 109:12017–12021. [PubMed: 22778397]
7. Hutten S, Kehlenbach RH. CRM1-mediated nuclear export: to the pore and beyond. Trends in cell biology. 2007; 17:193–201. [PubMed: 17317185]
8. Xu D, Farmer A, Chook YM. Recognition of nuclear targeting signals by Karyopherin-beta proteins. Current opinion in structural biology. 2010; 20:782–790. [PubMed: 20951026]
9. Xu D, Grishin NV, Chook YM. NESdb: a database of NES-containing CRM1 cargoes. Molecular biology of the cell. 2012; 23:3673–3676. [PubMed: 22833564]
10. Fung HY, Chook YM. Atomic basis of CRM1-cargo recognition, release and inhibition. Seminars in cancer biology. 2014
11. Iqbal K, Alonso Adel C, Grundke-Iqbal I. Cytosolic abnormally hyperphosphorylated tau but not paired helical filaments sequester normal MAPs and inhibit microtubule assembly. Journal of Alzheimer's disease : JAD. 2008; 14:365–370. [PubMed: 18688085]
12. Alami NH, et al. Axonal transport of TDP-43 mRNA granules is impaired by ALS-causing mutations. Neuron. 2014; 81:536–543. [PubMed: 24507191]
13. Lagier-Tourenne C, Polymenidou M, Cleveland DW. TDP-43 and FUS/TLS: emerging roles in RNA processing and neurodegeneration. Human molecular genetics. 2010; 19:R46–64. [PubMed: 20400460]
14. Winton MJ, et al. Disturbance of nuclear and cytoplasmic TAR DNA-binding protein (TDP-43) induces disease-like redistribution, sequestration, and aggregate formation. The Journal of biological chemistry. 2008; 283:13302–13309. [PubMed: 18305110]
15. Kawai Y, Garduno L, Theodore M, Yang J, Arinze IJ. Acetylation-deacetylation of the transcription factor Nrf2 (nuclear factor erythroid 2-related factor 2) regulates its transcriptional activity and nucleocytoplasmic localization. The Journal of biological chemistry. 2011; 286:7629–7640. [PubMed: 21196497]
16. Niture SK, Jain AK, Shelton PM, Jaiswal AK. Src subfamily kinases regulate nuclear export and degradation of transcription factor Nrf2 to switch off Nrf2-mediated antioxidant activation of cytoprotective gene expression. The Journal of biological chemistry. 2011; 286:28821–28832. [PubMed: 21690096]
17. Linker RA, et al. Fumaric acid esters exert neuroprotective effects in neuroinflammation via activation of the Nrf2 antioxidant pathway. Brain : a journal of neurology. 2011; 134:678–692. [PubMed: 21354971]
18. Jain AK, Bloom DA, Jaiswal AK. Nuclear import and export signals in control of Nrf2. The Journal of biological chemistry. 2005; 280:29158–29168. [PubMed: 15901726]
19. Kudo N, et al. Leptomycin B inactivates CRM1/exportin 1 by covalent modification at a cysteine residue in the central conserved region. Proceedings of the National Academy of Sciences of the United States of America. 1999; 96:9112–9117. [PubMed: 10430904]
20. Sun Q, et al. Nuclear export inhibition through covalent conjugation and hydrolysis of Leptomycin B by CRM1. Proceedings of the National Academy of Sciences of the United States of America. 2013; 110:1303–1308. [PubMed: 23297231]
21. Lapalombella R, et al. Selective inhibitors of nuclear export show that CRM1/XPO1 is a target in chronic lymphocytic leukemia. Blood. 2012; 120:4621–4634. [PubMed: 23034282]
22. Etchin J, et al. Antileukemic activity of nuclear export inhibitors that spare normal hematopoietic cells. Leukemia. 2013; 27:66–74. [PubMed: 22847027]
23. Recks MS, et al. Early axonal damage and progressive myelin pathology define the kinetics of CNS histopathology in a mouse model of multiple sclerosis. Clinical immunology. 2013; 149:32–45. [PubMed: 23899992]

24. Sakakibara K, et al. CBS9106 is a novel reversible oral CRM1 inhibitor with CRM1 degrading activity. Blood. 2011; 118:3922–3931. [PubMed: 21841164]
25. Bloss EB, Hunter RG. Hippocampal kainate receptors. Vitamins and hormones. 2010; 82:167–184. [PubMed: 20472138]
26. Basso DM, et al. Basso Mouse Scale for locomotion detects differences in recovery after spinal cord injury in five common mouse strains. Journal of neurotrauma. 2006; 23:635–659. [PubMed: 16689667]
27. Merkler D, Ernsting T, Kerschensteiner M, Bruck W, Stadelmann C. A new focal EAE model of cortical demyelination: multiple sclerosis-like lesions with rapid resolution of inflammation and extensive remyelination. Brain : a journal of neurology. 2006; 129:1972–1983. [PubMed: 16714315]
28. Chaudhary P, et al. Lipoic Acid Reduces Inflammation in a Mouse Focal Cortical Experimental Autoimmune Encephalomyelitis Model. (P1.221). Neurology. 2014; 82:P1, 221.
29. Li A, et al. Upregulation of CRM1 Relates to Neuronal Apoptosis after Traumatic Brain Injury in Adult Rats. Journal of molecular neuroscience : MN. 2013; 51:208–218. [PubMed: 23494640]
30. Mastroeni D, et al. Reduced RAN expression and disrupted transport between cytoplasm and nucleus; a key event in Alzheimer's disease pathophysiology. PloS one. 2013; 8:e53349. [PubMed: 23308199]
31. Nagara Y, et al. Impaired cytoplasmic-nuclear transport of hypoxia-inducible factor-1alpha in amyotrophic lateral sclerosis. Brain pathology. 2013; 23:534–546. [PubMed: 23368766]
32. Dormann D, Haass C. TDP-43 and FUS: a nuclear affair. Trends in neurosciences. 2011; 34:339–348. [PubMed: 21700347]
33. Kim JY, Casaccia P. HDAC1 in axonal degeneration: A matter of subcellular localization. Cell cycle. 2010; 9:3680–3684. [PubMed: 20930523]
34. Zhang J, Herrup K. Nucleocytoplasmic Cdk5 is involved in neuronal cell cycle and death in post-mitotic neurons. Cell cycle. 2011; 10:1208–1214. [PubMed: 21415596]
35. Sultan A, et al. Nuclear tau, a key player in neuronal DNA protection. The Journal of biological chemistry. 2011; 286:4566–4575. [PubMed: 21131359]
36. Ke YD, et al. Tau-mediated nuclear depletion and cytoplasmic accumulation of SFPQ in Alzheimer's and Pick's disease. PloS one. 2012; 7:e35678. [PubMed: 22558197]
37. Aggarwal A, Agrawal DK. Importins and exportins regulating allergic immune responses. Mediators of inflammation. 2014; 2014:476357. [PubMed: 24733961]
38. Pemberton LF, Paschal BM. Mechanisms of receptor-mediated nuclear import and nuclear export. Traffic. 2005; 6:187–198. [PubMed: 15702987]
39. Shriver LP, Dittel BN. T-cell-mediated disruption of the neuronal microtubule network: correlation with early reversible axonal dysfunction in acute experimental autoimmune encephalomyelitis. The American journal of pathology. 2006; 169:999–1011. [PubMed: 16936273]
40. Goldmann T, Prinz M. Role of microglia in CNS autoimmunity. Clinical & developmental immunology. 2013; 2013:208093. [PubMed: 23840238]
41. Campbell GR, Mahad DJ. Mitochondria as crucial players in demyelinated axons: lessons from neuropathology and experimental demyelination. Autoimmune diseases. 2011; 2011:262847. [PubMed: 21331147]
42. Stankiewicz JM, Kolb H, Karni A, Weiner HL. Role of immunosuppressive therapy for the treatment of multiple sclerosis. Neurotherapeutics : the journal of the American Society for Experimental NeuroTherapeutics. 2013; 10:77–88. [PubMed: 23271506]
43. Tedeholm H, et al. Time to secondary progression in patients with multiple sclerosis who were treated with first generation immunomodulating drugs. Multiple sclerosis. 2013; 19:765–774. [PubMed: 23124789]
44. Rawji KS, Yong VW. The benefits and detriments of macrophages/microglia in models of multiple sclerosis. Clinical & developmental immunology. 2013; 2013:948976. [PubMed: 23840244]
45. Koyama M, Matsuura Y. An allosteric mechanism to displace nuclear export cargo from CRM1 and RanGTP by RanBP1. The EMBO journal. 2010; 29:2002–2013. [PubMed: 20485264]

46. Vaguine AA, Richelle J, Wodak SJ. SFCHECK: a unified set of procedures for evaluating the quality of macromolecular structure-factor data and their agreement with the atomic model. Acta crystallographica. Section D, Biological crystallography. 1999; 55:191–205.

47. Bernard CC, et al. Myelin oligodendrocyte glycoprotein: a novel candidate autoantigen in multiple sclerosis. Journal of molecular medicine. 1997; 75:77–88. [PubMed: 9083925]

48. Stoppini L, Buchs PA, Muller D. A simple method for organotypic cultures of nervous tissue. Journal of neuroscience methods. 1991; 37:173–182. [PubMed: 1715499]

49. Vidaurre OG, et al. Cerebrospinal fluid ceramides from patients with multiple sclerosis impair neuronal bioenergetics. Brain : a journal of neurology. 2014; 137:2271–2286. [PubMed: 24893707]

50. la Cour T, et al. Analysis and prediction of leucine-rich nuclear export signals. Protein engineering, design & selection : PEDS. 2004; 17:527–536.

One Sentence Summary

Targeting the catalytic groove of exportin 1 prevents clinical progression in several mouse models of axonal damage by preserving axonal integrity.

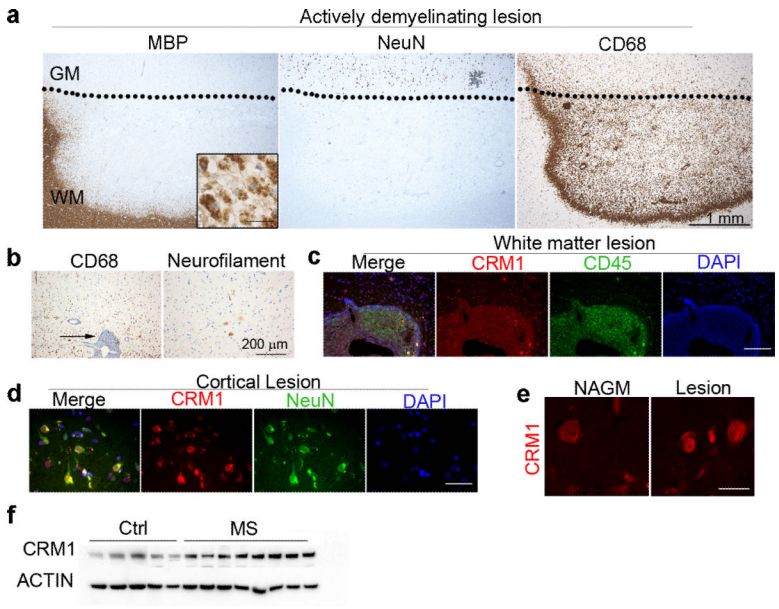

Figure 1. Expression of CRM1 in MS gray and white matter lesion areas

All pictures are derived from the same leukocortical MS lesion. (**a**) Immunohistochemical staining of a leukocortical MS lesion, which was characterized by staining for myelin basic protein (MBP), NeuN for neurons and CD68 for monocytes/microglia. The dotted line indicates the border between grey and white matter. Note the loss of myelin and the presence of myelin-laden phagocytes at the edges of the lesion (insert in the MBP staining panel; scale bar = 25 µm). CD68 positive cells were detected in gray and white matter, with higher numbers in the white matter part of the lesion. (**b**) The left panel depicts a perivascular infiltrate in the white matter part of the lesion and the arrow indicates the numerous C68+ positive cells within the infiltrate as well as in the parenchyma. Damaged neurons were identified by somatic staining for neurofilament. (**c**) The fluorescent images show at higher magnification the large inflammatory infiltrate located at the border between white and gray matter indicated by an arrow in (**b**). Numerous CD45 positive leukocytes (green) express CRM1 (red). Nuclei were counterstained with DAPI (blue); scale bar = 100 µm. Low (**d**) and high (**e**) magnification confocal images of lesional areas of MS gray matter and normal appearing gray matter stained for NeuN (green) to identify neurons and CRM1 (red). Scale bar = 40 µm for (**d**) and 15 µm for (**e**).(**f**) Western blot analysis of protein extracts of post-mortem human gray matter tissue prepared from non-neurological controls (n = 5) and MS patients (n = 8) which were probed with antibodies specific for CRM1, ACTIN was used as a loading control. Blots were cropped and full length images are presented in Supplementary Figure 11.

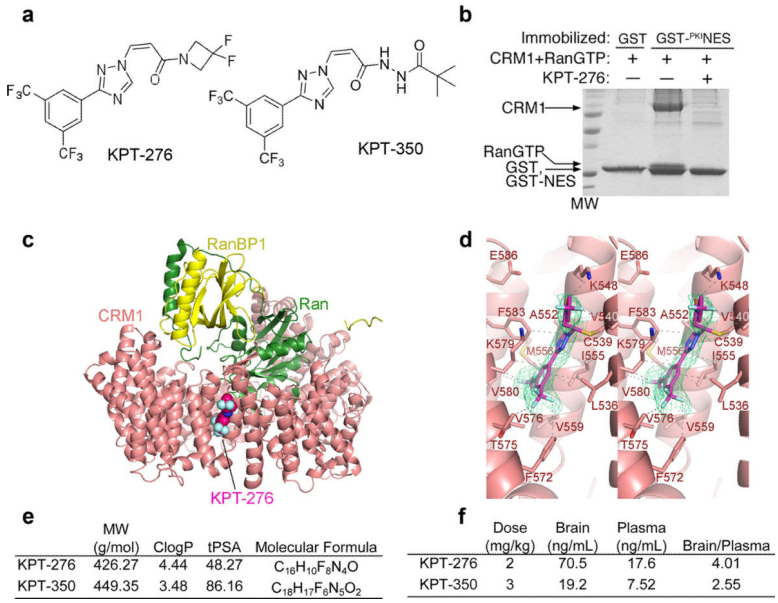

e

	MW (g/mol)	ClogP	tPSA	Molecular Formula
KPT-276	426.27	4.44	48.27	$C_{18}H_{10}F_8N_4O$
KPT-350	449.35	3.48	86.16	$C_{18}H_{17}F_6N_5O_2$

f

	Dose (mg/kg)	Brain (ng/mL)	Plasma (ng/mL)	Brain/Plasma
KPT-276	2	70.5	17.6	4.01
KPT-350	3	19.2	7.52	2.55

Figure 2. KPT selectively and covalently bind CRM1 and inhibit binding to NES with pharmacokinetic properties that favor blood brain barrier permeability

(**a**) Chemical structure of KPT-276 and KPT-350. (**b**) Inhibition of CRM1-NES binding by KPT-276 due to direct blockade of the NES binding groove. Pull-down assay of ~15 μg of 10 μM ^{Hs}CRM1 binding to either immobilized GST or GST-^{PKI}NES in the presence of RanGTP and either buffer or 100 μM KPT-276. (**c**) The 1.8 Å resolution crystal structure of KPT-276 bound to CRM1 showing KPT-276 binding in the NES-binding groove. (**d**) Magnified view of KPT-276 bound to CRM1 showing interactions between the inhibitor and CRM1 with the composite omit map of the inhibitor shown as a green mesh. (**e**) Pharmacological properties of KPT-276 and KPT-350 including molecular weight (MW), clogP (calculated logarithm of partition coefficient), topological polar surface area (tPSA) and molecular formula. (**f**) Pharmacokinetic properties of orally gavaged KPT-276 (2 mg/kg) and KPT-350 (3 mg/kg) in Sprague-Dawley rats.

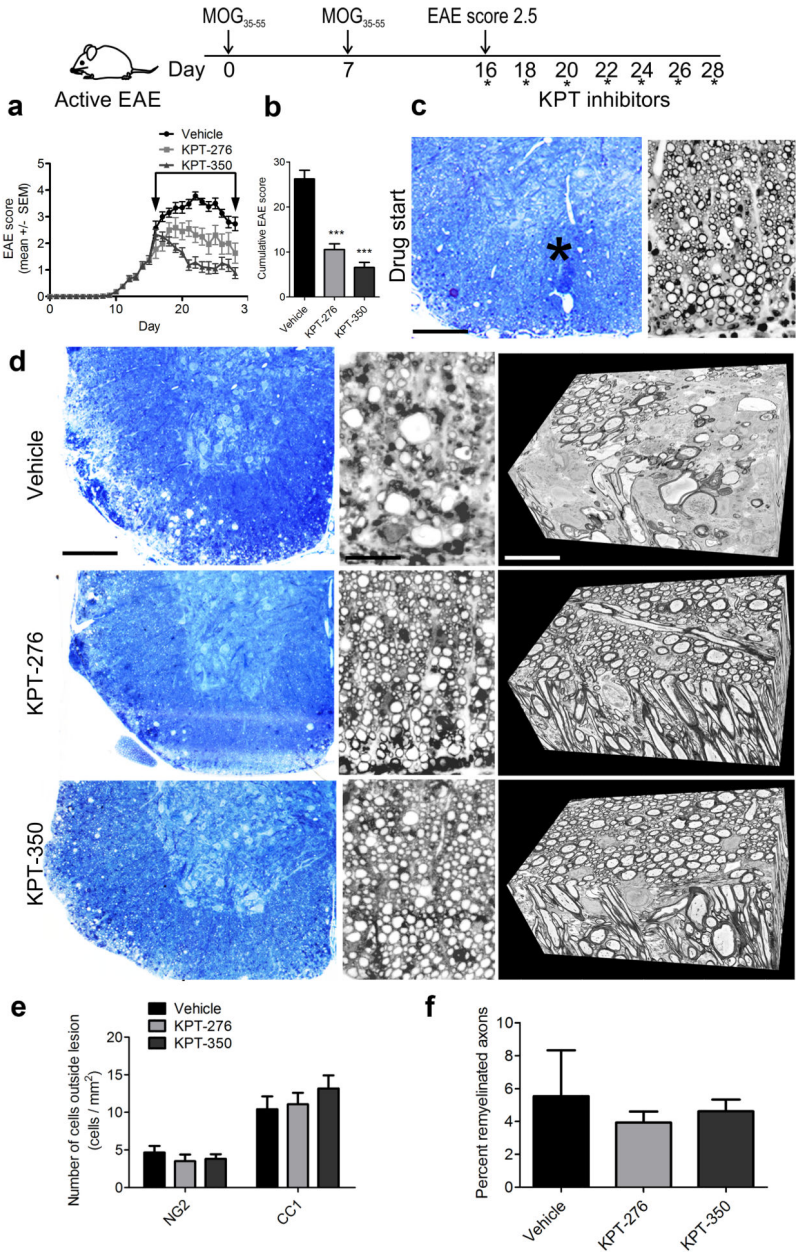

Figure. 3. Therapeutic treatment of EAE mice with KPT after the onset of hindlimb paralysis is associated with myelinated axon preservation

(**a**) Schematic diagram of treatment paradigm for therapeutic EAE. Disease course in mice with MOG_{35-55}-induced EAE treated with either vehicle, KPT-276, or KPT-350 starting at a clinical score 2.5; arrow indicates treatment window (n = 128 for vehicle, n = 101 for KPT-276, n = 110 for KPT-350), from three independent experiments. (**b**) Quantification of cumulative EAE score for the mice treated as described in (**a**). (**c**) Low and high magnification toluidine blue stained coronal sections from EAE spinal cord at treatment start. Inflammatory lesions are identified by asterisk. Scale bar = 150 μm in low magnification toluidine blue, 10 μm in high magnification. (**d**) Toluidine blue sections from vehicle, KPT-276 and KPT-350-treated animals, at treatment endpoint and corresponding

representative 3D-EM serially reconstructed data stacks. Scale bar = 150 μm in low magnification toluidine blue, 10 μm in high magnification, 2 μm in serial EM. (**e**) Quantification of immunofluorescence NG2- and CC1-positive cells outside of lesions from n = 3 animals per group, from two independent experiments. (**f**) Quantification of remyelinated axons in toluidine blue sections. Values represent mean ± SEM of three fields, from three independent experiments. Statistical differences in (**b**), (**e**), (**f**) were determined using one-way ANOVA with Dunnett's correction (***$p < 0.001$ vs. vehicle).

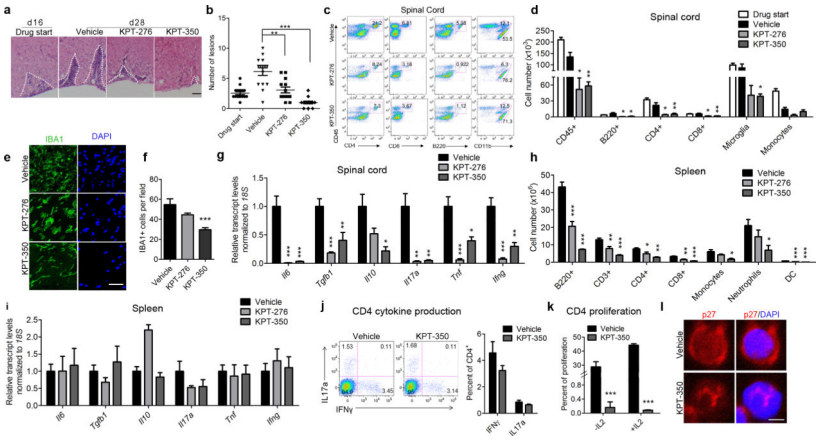

Figure 4. Therapeutic treatment of EAE mice with KPT reduces inflammatory burden in the spinal cord and impairs CD4 T cell proliferative capacity, but does not affect their ability to produce cytokines

(**a**) Histopathological characterization of inflammatory infiltrates, as detected in hematoxylin and eosin stained coronal sections from lumbar spinal cord of mice at treatment start time (d16), and end (d28); dotted lines delineate inflammatory lesions (scale bar = 1 mm). (**b**) Graphs representing the number of infiltrates in (**a**), n = 3 mice per condition, 5 sections per mouse from 2 independent experiments. (**c**) Representative FACS plots of CD4, CD8, B220 or CD11b cells in the spinal cord of treated mice in therapeutic vehicle, KPT-276 and KPT-350 mice. Numbers in FACS plots indicate percentage in live cell gate. (**d**) Quantification of cell numbers in spinal cords of vehicle, KPT-276, or KPT-350. Microglial cells were identified as $CD11b^{+}/CD45^{low}$ and monocytes as $CD11b^{+}/CD45^{high}$ (n = 4-6 treated mice per condition in two independent experiments). (**e**) $IBA1^{+}$ (green) stained sections from EAE spinal cord, sections were counterstained with DAPI (blue); scale bar = 100 μm. (**f**) Quantification of IBA1+ microglia from confocal sections in (**e**), n = 3 mice per group. (**g**) Relative transcript levels of cytokines in spinal cords of EAE mice therapeutically treated with either vehicle, KPT-276, or KPT-350, measured by qPCR and normalized to *18S* rRNA (n = 8 per condition, from two independent experiments). (**h**) Quantification by flow cytometry of splenic populations in vehicle, KPT-276 or KPT-350 treated mice. Monocytes were identified as $CD11b^{+}/CD115^{+}$, neutrophils as $CD11b^{+}/CD115^{-}$ and dendritic cells (DC) as $CD11c^{+}/MHCII^{high}$ (n = 3-4 mice per condition). (**i**) Relative transcript levels of cytokines in the spleen of treated mice with either vehicle, KPT-276, or KPT-350, measured by qPCR and normalized to *18S* rRNA n = 3 per condition. (**j**) Representative example of IFNγ and IL17a intracellular staining among splenic $CD4^{+}$ T cells from therapeutic treated vehicle and KPT-350 mice and quantification. Numbers in FACS plots indicate percentage in $CD4^{+}$ gate (n = 4 mice per group, representative of two biological replicate). (**k**) Quantification of $CD4^{+}$ T cell proliferation in cells treated with either vehicle or KPT-350 and stimulated with anti-CD3 and anti-CD28 in the presence and absence of IL-2 for 48 hours (***p = 0.001 for –IL2 and ***p = 0.0001). (**l**) Nuclear accumulation of the cell cycle inhibitor p27Kip1 (red) in CD4+ splenocytes acutely isolated from vehicle and KPT-350 treated EAE animals, cells were counterstained with DAPI (blue); scale bar = 3 μm. All graphs represent mean ± SEM. Statistical differences in panels (**b, d, f-i**) were determined using ANOVA with Dunnett's correction

(*p < 0.05, **p < 0.01, ***p < 0.001 vs. vehicle-treated animals). Statistical differences in (**j**), (**k**) were determined using independent t-tests with Bonferroni correction (***p < 0.001).

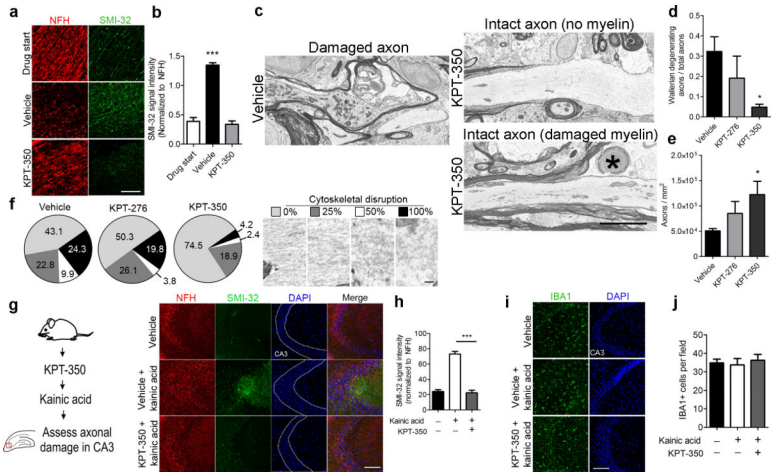

Figure 5. KPT inhibitors provide axonal protection in mouse models which are both dependent and independent of inflammation

(**a**) Representative spinal cord sections from therapeutically treated EAE mice stained for NFH (red), SMI-32 (green), scale bar = 50 μm. (**b**) Quantification of SMI-32 signal intensity relative to NFH from. (**c**) Representative EM images from three-dimensional reconstructed blocks showing degenerating axons from vehicle-treated EAE mice, and sections from KPT-350 mice depicting intact axons with no myelin, and intact axons with split myelin lamellae, (* indicates intra-lamellar myelin debris); scale bar = 1.0 μm. (**d**) Quantification from 3D-EM data sets of axons undergoing Wallerian degeneration normalized to total axons. (**e**) Quantification from 3D-EM data sets of total axons per mm^2. (**f**) Pie graphs representing the relative degree of cytoskeletal damage in axons from vehicle, KPT-276 or KPT-350 treated mice. Healthy axons were defined by 100% cytoskeletal arrangement. Axonal damage was then quantified based on the percentage of cytoskeletal disruption with 25% or 50% disruption as indicated by an absent, fragmented or aberrantly oriented cytoskeleton; 100% disruption when only a disrupted, or flocculent cytoskeleton were detected. At least 200 axons were counted per treatment group and at least n = 2 mice per group; scale bar = 0.1 μm. (**g**) Schematic diagram of *in vivo* kainic acid-induced neurotoxicity in mice. Representative confocal images of CA3 region of *in vivo* mouse hippocampus from mice treated with either vehicle or KPT-350 (7.5 mg/kg) for 1 hr followed by injection with kainic acid (2 mg/kg) for 18 hr. Coronal brain slices of hippocampus were stained with NFH (red), SMI-32 (green), DAPI (blue); scale bar = 100 μm. (**h**) Quantification of SMI-32 intensity. Values represent mean pixel intensity ± SEM of n=2 animals per group, from two independent experiments. (**i**) Representative $IBA1^+$ (green) stained sections of hippocampus, sections were counterstained with DAPI (blue); scale bar = 100 μm. (**j**) Quantification of (**i**). Bar graphs represent mean ± SEM. Statistical differences in: (**b**), (**h**), and (**j**) were determined using one-way ANOVA with Tukey's correction (**p < 0.01 vs. vehicle, ***p < 0.001 vs kainic acid); (**d**), (**e**) Kruskall-Wallis tests with Dunn's correction (*p < 0.05 vs. vehicle-treated controls, n=3 animals per group).

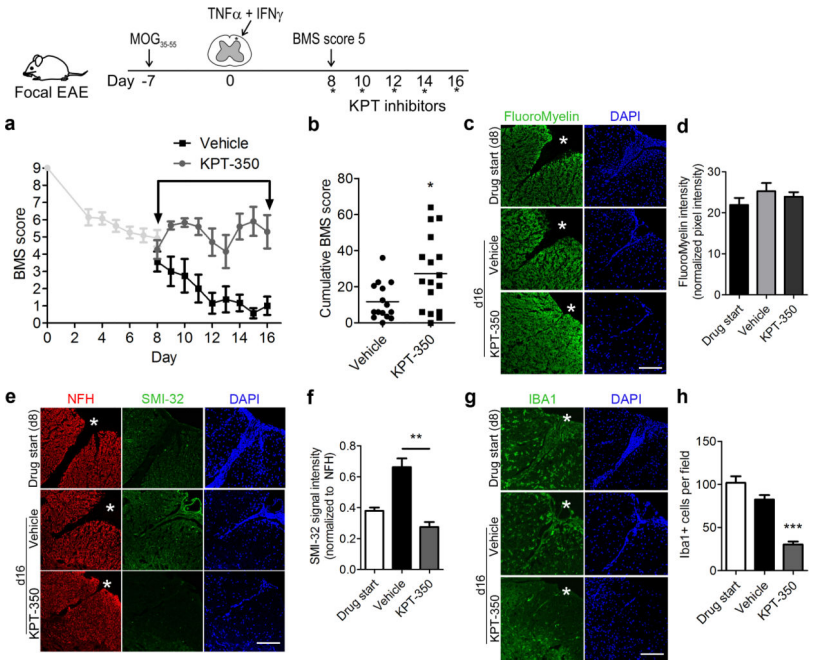

Figure 6. KPT inhibitors prevent locomotion decline and partially restore motor function in a localized EAE mouse model

(**a**) Schematic diagram of focal EAE model used to assess locomotor activity using the Basso Motor Scale (BMS). Locomotion of focal EAE mice were assessed daily using BMS; arrow indicates treatment window (n=3 for drug start; n = 11 for vehicle, n=12 for KPT-350), from three independent experiments. (**b**) Scatter plots depicting quantification of cumulative BMS score from (**a**) (*p = 0.0127). (**c**) Representative coronal spinal cord sections from focal EAE mice were stained with FluoroMyelin (green); scale bar = 200 μm. (**d**) Quantification of FluoroMyelin intensity from focal EAE animals. (**e**) Representative confocal images of axonal damage was assessed in coronal sections from focal EAE mice by staining with SMI-32 (green) and NFH (red); scale bar = 200 μm. (**f**) Quantification of SMI-32 intensity from (**e**). (**g**) IBA1^{+} (green) stained sections from EAE spinal cord, sections were counterstained with DAPI (blue); scale bar = 200 μm. (**h**) Quantification of IBA1+ microglia from confocal sections in (**g**), n = 3 animals per treatment group. Bar graphs represent mean ± SEM. Statistical differences in: (**b**) was determined using independent t-test (*p<0.05); (**f**) one-way ANOVA with Tukey's correction (**p < 0.01); (**d**), (**h**) one-way ANOVA with Dunnett's correction (***p<0.001 vs. drug start).

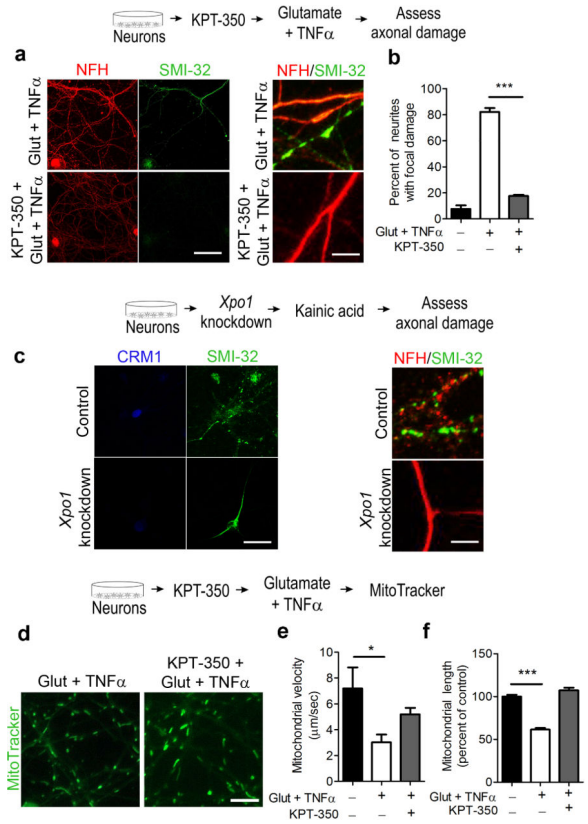

Figure 7. Treatment of cultured neurons with KPT-350 or knockdown of CRM1 prevents the induction of focal axonal damage and prevents damage in models independent of inflammation

(**a**). Representative low and high magnification images of rat hippocampal neurons treated with glutamate (50 μM) and TNFα (200 ng/mL) for 4 hr and stained with neurofilament NFH (red) to identify neuronal processes and SMI-32 (green) to detect damaged neurons with localized swellings. Scale bar = 25μm for low magnification and 15 μm for high magnification (**b**) Quantification of focal axonal damage expressed as percentage of neuronal processes with beading as shown in (**a**), n = 10 neurites per field, 10 fields per experiment, three independent biological replicates. (**c**) Representative confocal images of neurons infected with either control or *Xpo1* knockdown lentiviral particles. *Xpo1* knockdown was confirmed by staining for CRM1 (blue). Focal axonal damage was evaluated by staining neuronal cultures with neurofilament NFH (red) to identify neuronal processes and SMI-32 (green) to detect damaged neurites in neuronal cultures treated kainic acid. Scale bar = 25 μm for low magnification and 5 μm for high magnification (**d**) Representative still images of mitochondria from videos of cultured neurons stained with the live MitoTracker® Green FM dye; scale bar = 25 μm. (**e**) Quantification of mitochondrial velocity from (**d**), n = > 10 mitochondria per condition in three independent biological replicates. (**f**) Quantification of mitochondrial length from (**d**), n = 150 mitochondria per condition, from three independent experiments. Bar graphs represent mean pixel intensity ± SEM. Statistical significance in: (**b**) was determined using one-way ANOVA with Tukey's test (***p < 0.001 vs. Glut+TNFα) (**e**), (**f**) were determined using one-way ANOVA with Dunnett's correction (*p < 0.05, ***p < 0.001 vs. control).

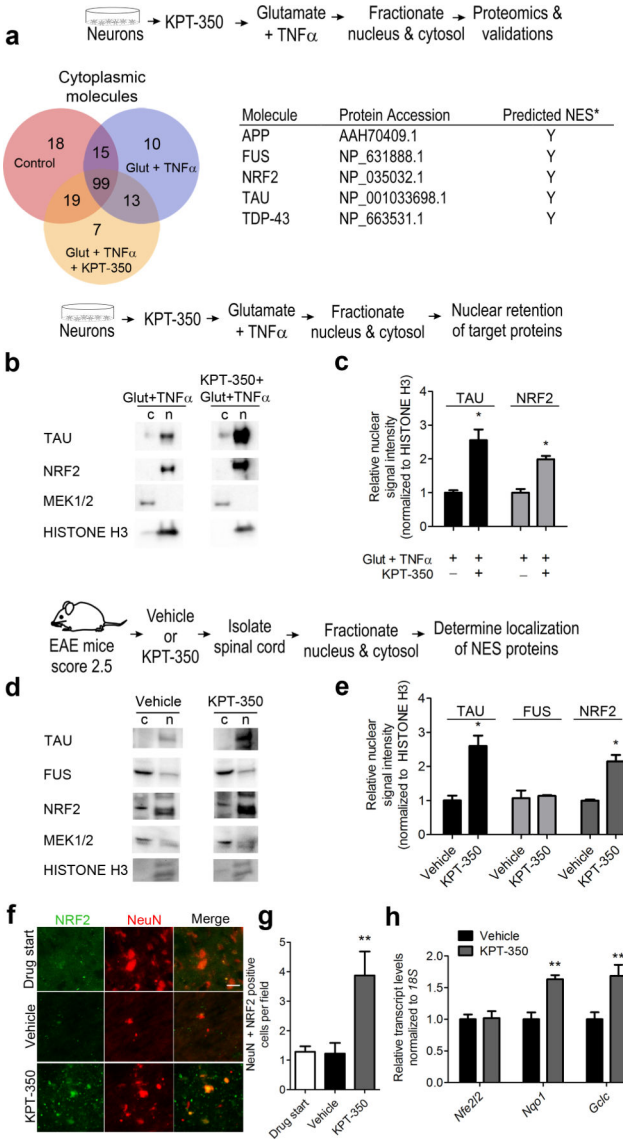

Figure 8. Proteomic screen of neurons treated with KPT-350 led to the identification of target molecules explaining the neuroprotective effect

(**a**) Schematic diagram of the methodology used to determine the mechanism of neuroprotection induced by KPT molecules. The Venn diagrams represents the cytoplasmic molecules identified from the proteomics analysis of neurons treated with vehicle, with glut +TNFα or KPT-350 + glutamate + TNFα. The table lists identified protein targets that contain predicted nuclear export sequences (NES) which were not enriched in the cytoplasmic compartment following treatment with glutamate + TNFα + KPT-350. The predicted NES was determined using NetNES 1.1 Server. (**b**) Schematic diagram of neuronal culture system used to validate proteomics targets. Validation of TAU and NRF2 as targets in cultured KPT-350 treated neurons. Western blot analysis of cytosolic [c] and nuclear [n] protein extracts from cultured cortical neurons treated with glut+TNFα or KPT-350+glut+TNFα. Antibodies for MEK1/2 and HISTONE H3 were used as internal controls for cytosolic and nuclear proteins, respectively (n = 3 samples per condition, two

independent experiments). Blots were cropped and full length images are presented in Supplementary Figure 12. (**c**) Quantification of the results in nuclear extracts from the experiments described in (**b**) (*p = 0.0341 for TAU and *p = 0.0213 for NRF2). (**d**) Schematic diagram of system used to validate nuclear retained targets in EAE mice. Validation of the KPT-350 targets in spinal cord extracts from treated mice. Western blots of cytosolic [c] and nuclear [n] protein extracts from the spinal cords of mice harvested after treatment with vehicle or KPT-350. Blots were probed with antibodies specific for TAU, FUS, and NRF2. MEK1/2 and HISTONE H3 were used both as loading controls and to verify correct cytosolic and nuclear fractionation, respectively (n = 3 samples per condition, two independent experiments). Blots were cropped and full length images are presented in Supplementary Figure 13. (**e**) Quantification of western blots of nuclear extracts as described in (**d**) (*p = 0.0413 for TAU and *p = 0.0257 for NRF2) . (**f**) Representative confocal images of EAE lumbar spinal cords from mice at treatment onset (drug start) or treated for 12 days with vehicle or KPT-350. Sections were stained with antibodies for NRF2 (green) and NeuN (red); scale bar = 20 μm, n = 3 fields per animal in twelve mice from two independent experiments. (**g**) Quantification of the number of NRF2/NeuN immunoreactive cells per field; n = 10 fields per animal, n = 6 mice per group in two independent experiments. (**h**) Transcript levels for *Nfe2l2* and the NRF2 target genes *Nqo1* and *Gclc* (n = 8 RNA samples per condition from two independent experiments, **p = 0.0010 for *Nqo1* and **p = 0.0021 for *Gclc*)). Bar graphs represent mean ± SEM. Statistical differences in (**c**), (**e**), (**g**), (**h**) were determined using independent t-tests, with Bonferroni correction (*p < 0.05, **p < 0.01 vs. vehicle).